Journal of
Materials Chemistry A

Accepted Manuscript

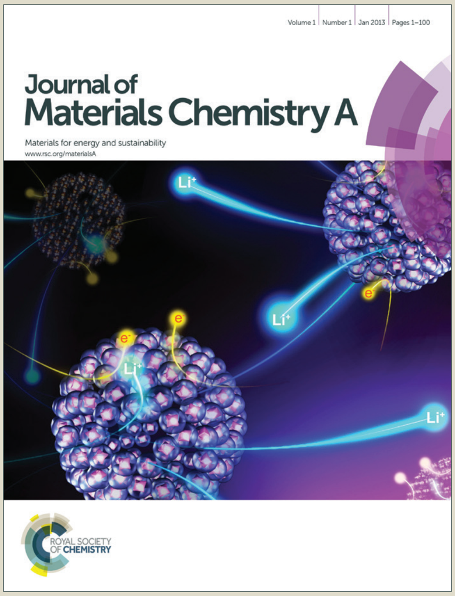

ROYAL SOCIETY
OF **CHEMISTRY**

www.rsc.org/materialsA

Dynamic Article Links ►

Cite this: DOI: 10.1039/c0xx00000x

www.rsc.org/xxxxxx

ARTICLE TYPE

Tetragonal tungsten bronze-type nanorod photocatalysts with tunnel structure: Ta substitution for Nb and overall water splitting

Ping Wang,[a] Larissa Schwertmann,[a] Roland Marschall[a,b] and Michael Wark*[a,c]

Received (in XXX, XXX) Xth XXXXXXXXX 20XX, Accepted Xth XXXXXXXXX 20XX

DOI: 10.1039/b000000x

Tetragonal tungsten bronze-type tantalum (Ta) substituted $Sr_2KNb_5O_{15}$ nanorod photocatalysts with tunnel structure were prepared by a facile and low-cost molten salt method using potassium chloride (KCl) at 850 °C for only 2 h. Although all native photocatalysts did not possess any detectable activity in pure water splitting, after deposition of NiO_x (double-layered Ni/NiO) as co-catalysts, samples of $Sr_2KNb_5O_{15}$ and $Sr_2KTa_5O_{15}$ can split pure water into H_2 and O_2 in a stoichiometric amount (≈ 2:1), which can be ascribed to the improved charge carrier separation and transfer in the presence of NiO_x. Furthermore, Ta substitution effects on the photocatalytic behaviour were systematically investigated for hydrogen production by aqueous methanol reforming. The average H_2 formation rates of $Sr_2KNb_{5-x}Ta_xO_{15}$ first decrease with tantalum substitution for $x < 2.5$, presumably due to a decreased amount of absorbed photons and an obvious reduction of their exposed surface areas, whereas the activity is significantly improved for samples containing more Ta ($x > 2.5$) and especially the fully substituted $Sr_2KTa_5O_{15}$. This can be explained by a stronger driving force for photogenerated conduction band electrons to reduce water.

Introduction

Photocatalytic water splitting and hydrogen production by semiconductor photocatalysis for converting solar energy into chemical energy has drawn ever-growing interest in both science and engineering fields.[1, 2] During the past few years, several types of semiconductor photocatalysts such as bulk-type simple oxides (TiO_2, Nb_2O_5, Ta_2O_5, ZnO and ZrO_2, etc.) as well as perovskite-type oxides ($SrTiO_3$, $K_4Nb_6O_{17}$, $NaTaO_3$, and $A_2La_2Ti_3O_{10}$, (A=Ca, Sr, and Ba), etc.) have been widely studied.[3-6] It is well known that the superior photocatalytic ability of layered oxides can be attributed to the unique structure, compared to the above-mentioned bulk-type oxides.[7]

The past two decades have also witnessed great efforts on the synthesis of tunnel-structured oxides, such as $BaTi_4O_9$ and $A_2Ti_6O_{13}$ (A = Na, K, Rb), etc.[8, 9] The deficient perovskite tetragonal tungsten bronze-type (TTB) niobates $(A1)_4(A2)_2(A3)_4Nb_{10}O_{30}$, consisting of corner-sharing NbO_6 octahedra arrays and three different tunnels (A1, A2 and A3) for cation filling, have been widely investigated as ferroelectric and piezoelectric materials in view of their large spontaneous polarization and high dielectric constants.[10-14] They also exhibit dominant electron-hole separation and transport via static electric fields between structure-induced dipole moments in distorted metal-oxygen polyhedra. Therefore, a slight structural modification by altering the cation-site occupancy has a dramatic effect on the charge mobility. However, to our knowledge except the paper by Wu, et al,[15] there have been no reports on photocatalytic properties of the modified tunnel-structure bronze-type niobates.

In principle on all the three cation positions A1, A2 and A3 a cation exchange can be done, but since recent studies in niobate/tantalate systems have shown that the substitution of the Nb site with tantalum (Ta) could considerably improve the photocatalytic activity[16-18], we concentrated on this substitution. However, most reports of substitution effects are focused on the photodegradation of organic compounds. It still remains a great challenge to directly split water into H_2 and O_2 and to determine the variation of the Ta substitution induced-structure properties and photocatalytic behaviour. In the present work, by employment of a simple and cost-effective molten salt technique, the $Sr_2KNb_{5-x}Ta_xO_{15}$ nanorod photocatalysts with different Nb/Ta substitution ratios were synthesized. The Ta substitution effect on the photocatalytic behaviour for photocatalytic hydrogen production from methanol reforming was systematically investigated.

Experimental

Photocatalysts preparation

Powders of $Sr_2KNb_{5-x}Ta_xO_{15}$ with x= 0, 1, 2.5, 4 and 5 were prepared by molten salt method.[19] $SrCO_3$ (≥99.99%, Aldrich), K_2CO_3 (>99.9%, Alfa Aesar), Nb_2O_5 (99.99%, Alfa Aesar), and Ta_2O_5 (99.85%, Alfa Aesar) were used as starting materials. The desired stoichiometric molar ratios of the starting materials were ground together with potassium chloride (KCl: 99.5%, Honeywell Riedel-de Haën) at a weight ratio of 1:2. The well-mixed powders were heated at different calcination temperatures for 2 h in air using a corundum crucible. After cooling down to room temperature, the mixture was intensively washed with distilled water in order to remove any residual salts and then dried in air at 80 °C. The 1.0 wt% NiO_x loaded samples were prepared by impregnation method:[20, 21] the respective powders were dispersed in a suitable amount of $Ni(NO_3)_2$ (99.9985%, STREM Chemicals) solution and heated under constant stirring until the water was completely evaporated. The resulting powder was dried at 80 °C in air, followed by calcination at 200 °C for 2 h, and further treated by reduction under H_2 flow at 300 °C for 2 h and re-oxidation under O_2 flow at 200 °C for 1 h.

Characterization

The X-ray diffraction (XRD) patterns of all samples were recorded with a PANalytical MPD diffractometer using Cu-Kα radiation (λ= 0.1541 nm), and the data were collected from 10° to 60° (2θ). Static N_2 physisorption measurements were carried out at -196 °C using an Autosorb-1MP Quantachrome system and samples were degassed at 200 °C for 6 h before the measurements. The UV-Vis diffuse reflectance spectra were measured using MgO as a reference on a UV/Vis Varian Cary 4000 spectrophotometer. Band gap energies were calculated by analysis of the Tauc-plots resulting from Kubelka-Munk transformation of diffuse reflectance spectra. Powder samples were sputter-coated with a thin layer of Au particles and then examined in scanning electron microscopes (SEM) using a LEO (Zeiss) 1530 Gemini field-emission. The transmission electron microscope (TEM) images were recorded by a Philips/FEI Tecnai F20 S-TWIN TEM instrument operating at 200 kV.

Photocatalytic activity for H_2 production

Photocatalytic reactions were performed in a typical double-walled inner irradiation-type quartz reactor connected to a closed gas evolution system.[19, 22] The reaction temperature was maintained at 10 °C to prevent any thermal catalytic effect with a double-walled quartz jacket filled with a flow of cooling water from a thermostat (LAUDA). A 500 W Hg mid-pressure immersion lamp (Peschl UV-Consulting) was used as a light source. High-purity Argon (6.0) was used as carrier gas for the reaction products, of which continuous gas flow was set to 50 NmL/min controlled by a Bronkhorst mass flow controller. The evolved gases were analyzed online using a multi-channel analyzer (Emerson) equipped with a detector for the determination of the concentration of hydrogen (thermal conductivity detector), oxygen (paramagnetism) and carbon dioxide (IR). In a typical run, 0.1 g of photocatalyst powder was suspended in 500 mL distilled water. In case of photocatalytic methanol reforming, an additional 50 mL of methanol was added. Prior to irradiation, the whole system including the photocatalysts was purged with argon to remove air completely.

Results and Discussion

Synthesis of materials Optical and physical properties

In order to determine the optimum calcination temperature, $Sr_2KTa_5O_{15}$ was prepared under different calcination temperatures from 850 to 1050 °C (higher than the melting point of KCl, 774 °C) and the photocatalytic activity of these samples was probed by photocatalytic methanol reforming for H_2 production. As shown in Figure 1, the diffraction peaks of the $Sr_2KTa_5O_{15}$ (JCPDS 40-0345) become sharper and stronger with increasing temperature, indicating the increase of the average crystallite size and the improvement of the crystallinity of $Sr_2KTa_5O_{15}$ crystals. As shown in Table 1, the sample calcined at 850 °C shows a BET surface area of 8.5 m^2/g, and an increase in calcination temperature resulted in the significantly decreased surface areas of 5.3 and 2.7 m^2/g for samples calcined at 950 °C and 1050 °C, respectively. Presumably enhanced particle growth results in a loss of active surface sites with increasing temperature, leading to an increasingly detrimental effect on the photoactivity for H_2 production. Therefore, we chose for the preparation of the samples with different Nb/Ta ratios $Sr_2KNb_{5-x}Ta_xO_{15}$ (x= 0, 1, 2.5, 4 and 5) a temperature of 850 °C.

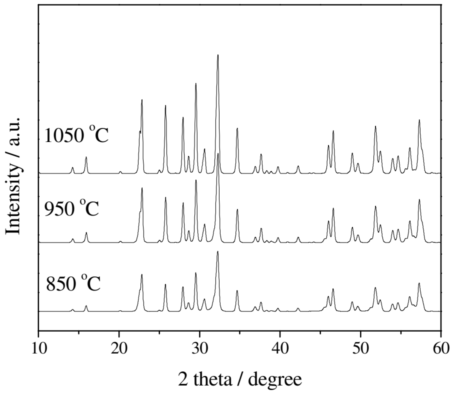

Figure 1. XRD patterns of typical $Sr_2KTa_5O_{15}$ samples synthesized with different calcination temperatures for 2 h.

Table 1. Effect of calcination temperature on BET surface area and photocatalytic activity for H_2 production.

Temperature (°C)	BET area (m^2/g)[a]	Rate of H_2 (mmol/h)[b]
850	8.5	1.24
950	5.3	1.23
1050	2.7	1.14

[a] measured by the Brunauer-Emmett-Teller (BET) method; [b] reaction conditions: 0.1 g of photocatalysts; 50 mL of methanol dissolved in 500 mL of water; 500W Hg lamp.

Structural properties

X-ray powder diffraction patterns of $Sr_2KNb_{5-x}Ta_xO_{15}$ (x= 0, 1, 2.5, 4 and 5) with different molar Nb/Ta ratios prepared at 850 °C for 2 h are shown in Figure 2. All the powders are well-crystallized and no significant shifts are observed in the diffraction patterns. This indicates that Ta^{5+} has diffused into the tetragonal tungsten bronze (TTB) structure to form a solid solution in which Ta^{5+} occupies the Nb lattice sites, because the effective ionic radii of Nb^{5+} and Ta^{5+} ions in the $Sr_2KNb_{5-x}Ta_xO_{15}$ are similar (64 pm), and on the contrary, the effective ionic radius of the Ta^{5+} ion is remarkably smaller than those of the Sr^{2+} ion and the K^+ ion.[23] As shown in Figure 2a, the pattern of our $Sr_2KNb_5O_{15}$ can be indexed to a TTB structure on basis of the reported data of bulk $Sr_2KNb_5O_{15}$ crystals (JCPDS 34-0108, space group *P4bm* belonging to the point group 4mm). However, the most intense reflection is (410), instead of (311, 420), and the intensity of (211) reflection decreases by more than half. This agrees very well with reported results,[24-26] and can be attributed to the anisotropic growth of the $Sr_2KNb_5O_{15}$ particles leading to a strong (001) orientation. It is important to note that some unknown impurity (< 3%) was observed for $Sr_2KNb_5O_{15}$, as indicated by the arrows in Figure 2a. Interestingly, no impurity peaks were detected with increasing x and the phenomenon of the preferred (001) orientation growth gradually began to be weakened for these solid solutions, indicating that the anisotropic grain growth is inhibited by Ta^{5+} substitution. After complete substitution of Ta^{5+} for Nb^{5+}, the $Sr_2KTa_5O_{15}$ phase was derived according to the JCPDS 40-0345. The diffraction peak at about 46.3° splits into two peaks (Figure 2b). This suggests that when substituting Nb^{5+} with Ta^{5+}, the crystal structure transition to a symmetric center appeared from tetragonal point group 4mm to tetragonal point group 4/mmm), in good agreement with the literature.[27, 28]

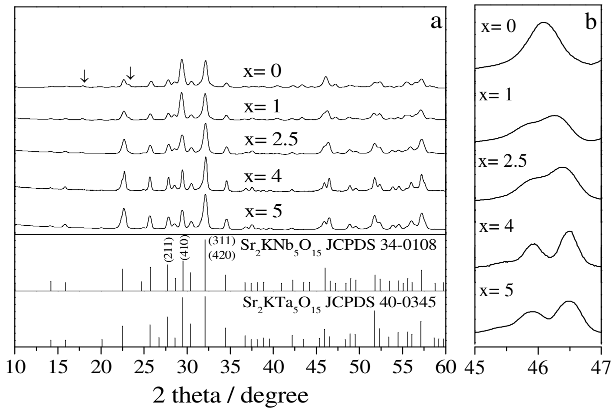

Figure 2. a) XRD patterns of $Sr_2KNb_{5-x}Ta_xO_{15}$ with x=0, 1, 2.5, 4 and 5 prepared at 850 °C for 2 h, b) Enlarged XRD patterns of the $Sr_2KNb_{5-x}Ta_xO_{15}$ ranging from 2θ = 45°-47°.

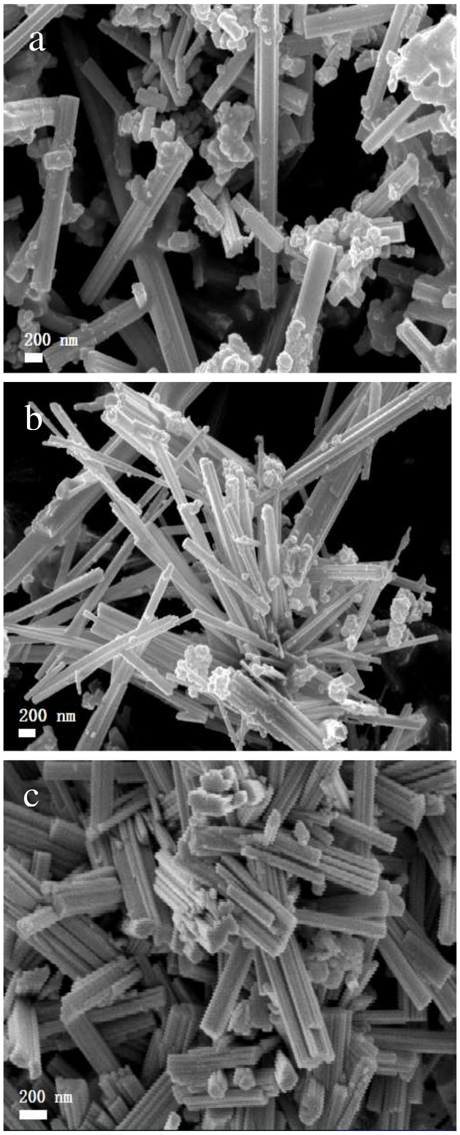

Figure 3. Representative SEM images of $Sr_2KNb_5O_{15}$ nanorods (a) $Sr_2KNb_{2.5}Ta_{2.5}O_{15}$ (b) and $Sr_2KTa_5O_{15}$ nanorods (c), respectively.

Representative SEM images of $Sr_2KNb_5O_{15}$ (a), $Sr_2KNb_{2.5}Ta_{2.5}O_{15}$ (b) and $Sr_2KTa_5O_{15}$ (c) samples are shown in **Error! Reference source not found.**. The samples display a nanorod-shaped morphology with the diameters in the range of 100-400 nm and the lengths up to a few microns, suggesting that the eutectic KCl salt favors the formation of nanorod morphology. With increasing Ta/Nb ratio most of the nanorods become more uniform in size, but also more agglomerated, and grow shorter in length, implying that the anisotropic grain growth can be to some extent be suppressed by the Ta^{5+} substitution, which is in accordance with the XRD analysis. A similar suppression caused by Ta^{5+} substitution was also found in other ceramic systems like $(K_{0.44}Na_{0.52}Li_{0.04})(Nb_{0.96-x}Ta_xSb_{0.04})O_3$, and $Sr_{0.53}Ba_{0.47}Nb_{2-x}Ta_xO_6$.[29, 30]

The microstructure, the lattice parameters and growth properties of the $Sr_2KNb_5O_{15}$ and $Sr_2KTa_5O_{15}$ nanorod samples were further studied by TEM, high-resolution TEM (HRTEM), and selected area electron diffraction (SAED). Figure 4a shows a TEM image of a typical $Sr_2KNb_5O_{15}$ nanorod at low magnification. The HRTEM image of the $Sr_2KNb_5O_{15}$ sample taken from the top part of the $Sr_2KNb_5O_{15}$ nanorod (as marked by a white rectangle in Figure 4a) and the corresponding SAED pattern are presented in Figure 4b and Figure 4c, respectively. The lattice fringes of the $Sr_2KNb_5O_{15}$ [001] and [400] planes are found to be about 0.39(0) nm and 0.31(2) nm, respectively and the SAED pattern can be assigned to tetragonal $Sr_2KNb_5O_{15}$ single crystals with the electron beam closely parallel to [010] direction. These observations unambiguously indicate that the $Sr_2KNb_5O_{15}$ nanorod is a high quality single crystal with tetragonal structure, grown along the [001] direction (marked by a white arrow in Figure 4b).

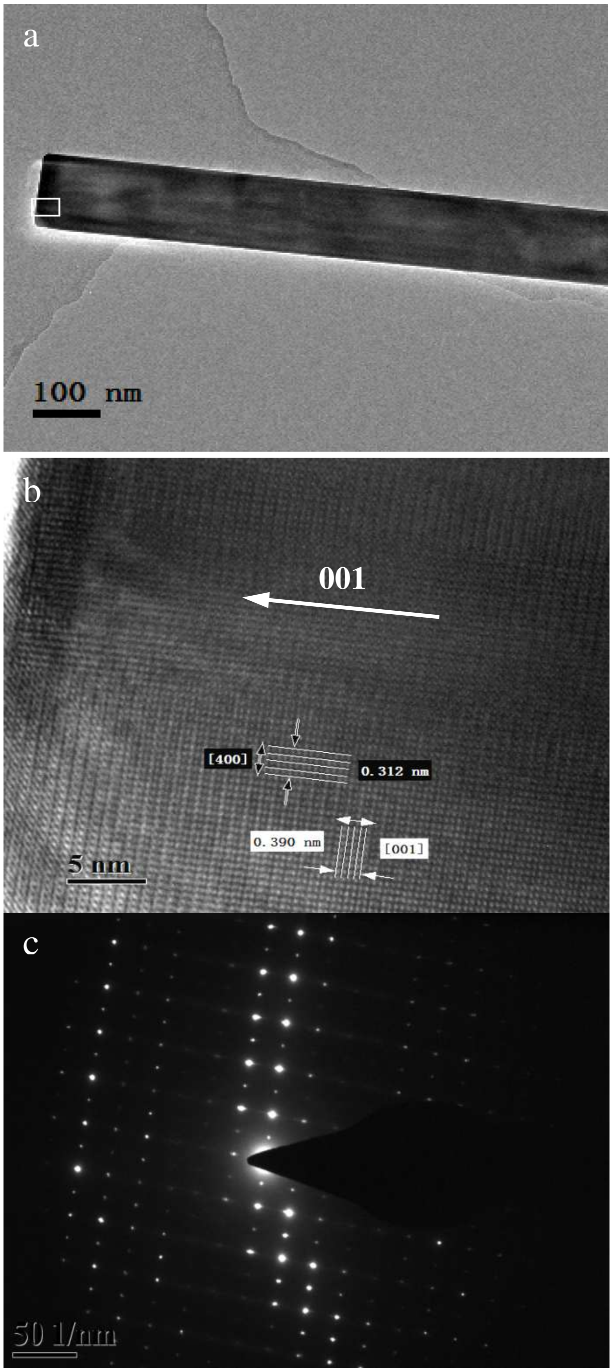

Figure 4. TEM images of the $Sr_2KNb_5O_{15}$ sample: (a) Low-magnification TEM image of a typical $Sr_2KNb_5O_{15}$ nanorod, (b) HRTEM taken from the top part of the $Sr_2KNb_5O_{15}$ nanorod as marked by a white rectangle in (a), the white arrow indicates growth direction of the $Sr_2KNb_5O_{15}$ nanorod along the [001] facet planes, (c) corresponding SAED pattern.

A typical $Sr_2KTa_5O_{15}$ nanorod can be observed in the low-magnification TEM image of Figure 5a. The HRTEM image in Figure 5b, which corresponds to the area marked by a white rectangle in Figure 5a, shows the same crystal planes and the same growth direction (as indicated by a white arrow) as illustrated in Figure 4b. Therefore, clear evidence for preferential growth direction of $Sr_2KNb_5O_{15}$ and $Sr_2KTa_5O_{15}$ nanorod samples could be further found and both of them have the same [001] growth direction. Therefore, it is suggested that the use of molten salt as a reaction medium plays a dominant role for the formation of nanorod morphology and their preferential growth, while presumably the growth inhibition caused by Ta substitution in these Ta substituted samples, as observed in above XRD and SEM results, is limited.

Figure 5c shows a representative TEM image of a typical 1.0 wt.% NiO_x loaded $Sr_2KTa_5O_{15}$ sample. It can be clearly seen that distinguishable nano-NiO_x co-catalyst particles are anchored on an individual $Sr_2KTa_5O_{15}$ nanorod. The nano-NiO_x co-catalyst particles consist of a solid Ni metal core and a brighter NiO outer layer. Furthermore, the inset on the lower right shows a lattice resolved HRTEM image of a nano-NiO_x particle, in which the lattices of the out layer-cubic NiO can be determined to be the [111] and [200] crystal planes with d-spacings of 0.24 nm and 0.21 nm, respectively. The results demonstrate that the double-layered structure of metallic Ni and metal oxide NiO is created on the surface of the $Sr_2KTa_5O_{15}$ nanorods photocatalyst by reduction-reoxidation processes. The formation of a Ni metal at the surface of photocatalyst results in the formation of a Schottky contact at the interface, and thus provides an opportunity to facilitate electron transport to the NiO shell to enhance the photocatalytic activity of the photocatalysts for overall water splitting as will be discussed below.

Optical and physical properties

The UV-Vis diffuse reflectance spectra of $Sr_2KNb_{5-x}Ta_xO_{15}$ with x= 0, 1, 2.5, 4 and 5 are shown in Figure 6a. The absorption edges of $Sr_2KNb_{5-x}Ta_xO_{15}$ obviously shift to shorter wavelengths with increasing Ta content. On basis of Kubelka–Munk transformation of the diffuse reflectance spectra, the band-gap energies from Tauc plots were larger than the apparent band-gap energies if direct transition is assumed for light absorption by the samples. As indicated in Figure 6b, the assumption of indirect transition is in good agreement with apparent band gap energies, thus suggesting that the as-prepared oxides are indirect band gap semiconductors. Figure 6c shows the band gaps of $Sr_2KNb_5O_{15}$, $Sr_2KNb_4Ta_1O_{15}$, $Sr_2KNb_{2.5}Ta_{2.5}O_{15}$, $Sr_2KNb_1Ta_4O_{15}$ and $Sr_2KTa_5O_{15}$ being estimated to about 3.19, 3.24, 3.32, 3.51 and 3.89 eV, respectively. The band gap of $Sr_2KNb_5O_{15}$ is almost consistent with the reported value (3.24 eV).[15] The data indicate that the band gaps do not linearly increase with the Ta substitution; for high Ta contents the band gap widening is more prominent.

On the other hand, the BET surface areas of $Sr_2KNb_{5-x}Ta_xO_{15}$ with x= 0, 1, 2.5, 4 and 5 decrease almost linearly with the substitution of Ta, as shown in Figure 6c. The surface area of as-prepared $Sr_2KNb_5O_{15}$ (19.1 m^2/g) was improved by more than 60 times compared with that of the sintered sample (0.31 m^2/g) by the conventional solid state reaction method,[15] which may provide more active sites, reduce the recombination of photogenerated electron-hole pairs, and thus greatly enhance photocatalytic efficiency. This can be ascribed to the lower reaction temperature and the shorter reaction times (at 850 °C for 2 h) possible due to the intimate contacts in the molten salt moderated reaction.[19, 31, 32]

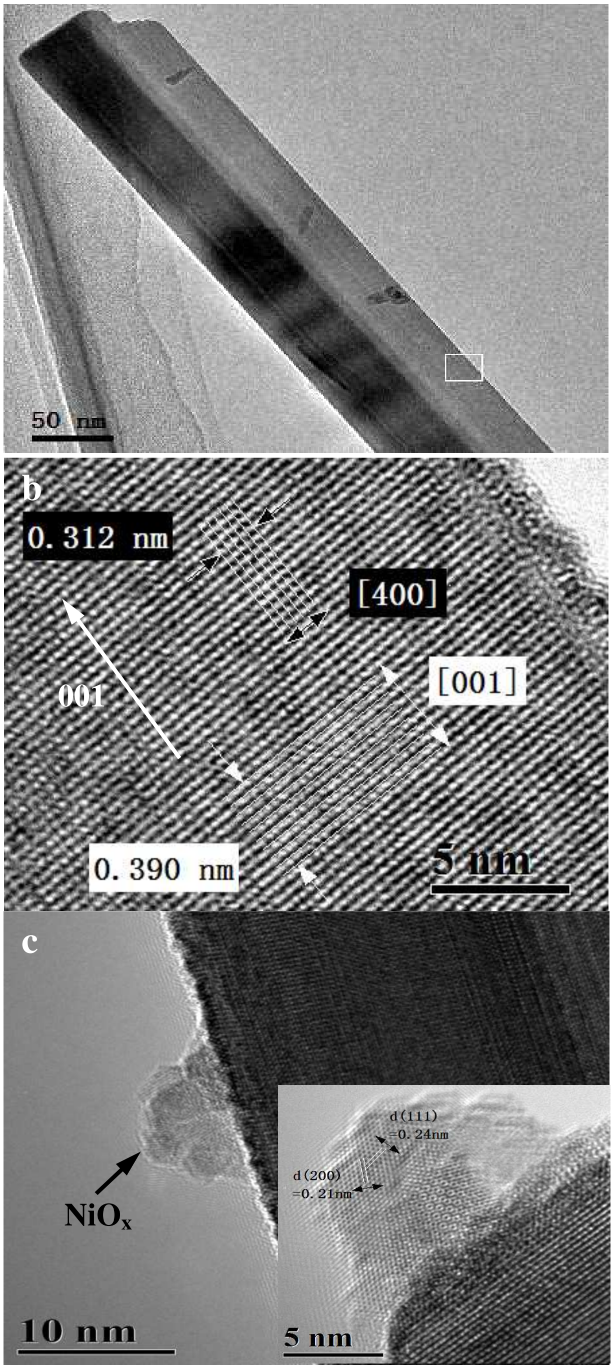

Figure 5. TEM images of the $Sr_2KTa_5O_{15}$ sample: (a) Low-magnification TEM image of a typical $Sr_2KTa_5O_{15}$ nanorod, (b) HRTEM taken from the edge of the $Sr_2KTa_5O_{15}$ nanorod as marked by a white rectangle in (a). The white arrow indicates growth direction of the $Sr_2KTa_5O_{15}$ nanorod along the [001] facet planes, (c) The TEM image of the 1.0 wt.% NiO_x loaded $Sr_2KTa_5O_{15}$ nanorod with inset of a NiO_x particle.

The band structure of photocatalysts is one of the important factors affecting the photonic efficiency. The valence band (VB) potentials of all $Sr_2KNb_{5-x}Ta_xO_{15}$ solid solutions should be quite similar because of the same crystal structure and the same orbitals (O 2p orbitals) comprising the VB. Thus, the difference of band gap energies is due to the orbitals forming the conduction band (CB). According to the report by Scaife,[33] for oxides containing no partly filled d-levels, the following equation can be used to approximately determine the flat band potential:

$$V_{fb}(NHE) = 2.94 - E_g \qquad (1)$$

where V_{fb} and E_g represent a flat band potential and a band gap, respectively. The band structures of $Sr_2KNb_{5-x}Ta_xO_{15}$ with x= 0, 1, 2.5, 4 and 5 are schematically illustrated in Figure 7. The CB of $Sr_2KNb_5O_{15}$ consists of Nb 4d, while that of $Sr_2KTa_5O_{15}$ is from Ta 5d. The CB formed by the empty Ta 5d orbitals lies at a considerably more negative potential than the Nb 4d orbitals. Thus, with increasing Ta substitution, the larger band gap will lead to the decreased amount of absorbed photons. On the contrary, it also means that the CB potential becomes more negative than the water reduction potential (<0 V vs. NHE at pH 0), suggesting that the driving force of $Sr_2KNb_{5-x}Ta_xO_{15}$ for water reduction by electrons in the CB becomes larger, thus promoting the transfer of photoelectrons. It can be concluded that the Ta substitution molar ratio has a great effect on the band structures and thus plays a crucial role in determining the efficiency of H_2 production.[34] Furthermore, the bottom level of the CB was much more negative than the reduction potential of H^+/H_2 (0 eV), while the top level of the VB was more positive than the oxidation potential of O_2/H_2O (+1.23 eV). It is therefore reasonable to infer that these photocatalysts might be able to split water into H_2 and O_2 by the appropriate excited energy.

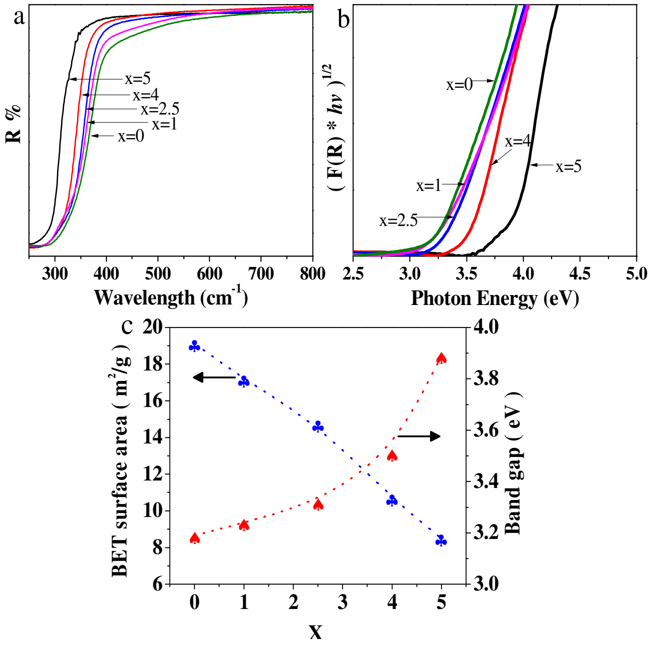

Figure 6. (a) UV-Vis diffuse reflection spectra of $Sr_2KNb_{5-x}Ta_xO_{15}$ with x= 0, 1, 2.5, 4 and 5, (b) Tauc plots (for indirect band gap transition) calculated from the Kubelka-Munk transformation, and (c) Band gap energies and BET surface areas of $Sr_2KNb_{5-x}Ta_xO_{15}$ with x= 0, 1, 2.5, 4 and 5, respectively.

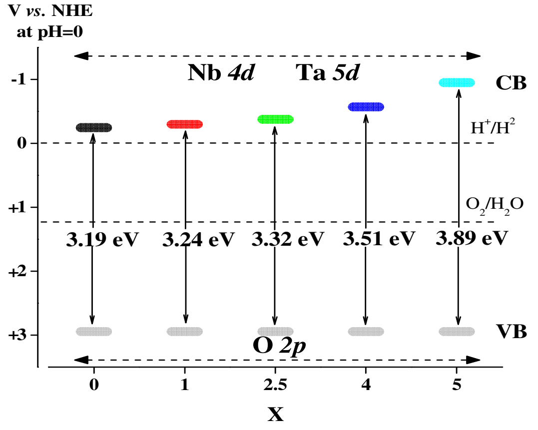

Figure 7. A schematic illustration of band structures of $Sr_2KNb_{5-x}Ta_xO_{15}$ with x= 0, 1, 2.5, 4 and 5.

Effect of Ta substitution on photocatalytic H_2 production by reforming of aqueous methanol solution

The photocatalytic H_2 production rates over co-catalyst-free $Sr_2KNb_{5-x}Ta_xO_{15}$ with x=0, 1, 2.5, 4 and 5 from photocatalytic reforming of methanol are shown in Figure 8. Note that the activities of photocatalysts with different Ta substitution molar ratio were compared by the average rate of H_2 production in the first 1 h and the same photocatalytic trend can be obtained by at least three repeated measurements. For comparison, commercial TiO_2 nanoparticles (Evonik P25) were also tested for photocatalytic H_2 production under the same conditions. The $Sr_2KNb_{5-x}Ta_xO_{15}$ solid solutions photocatalysts exhibited superior photocatalytic activity than P25. And it is clearly seen that the photocatalytic activity of $Sr_2KTa_5O_{15}$ is much higher than that of $Sr_2KNb_5O_{15}$. With the increased content of Ta substitution, the average formation rates of H_2 decreased first, the lowest activity was observed for the $Sr_2KNb_{2.5}Ta_{2.5}O_{15}$, and then began to increase in the case of $x > 2.5$. It might be possible that the crystal sizes and crystallinity of the solid solutions negligibly influence the photocatalytic activity because their crystal sizes and high crystallinity were not significantly changed by Ta substitution from the XRD results. Therefore, the obvious decrease of H_2 formation rate ($x < 2.5$) can be related to the decreased number of absorbed photons and lower specific surface areas. With higher Ta substitution ($x > 2.5$), the increase of H_2 formation rate can be mainly attributed to the stronger driving force and more effective photoelectron transfer from the CB as described above.

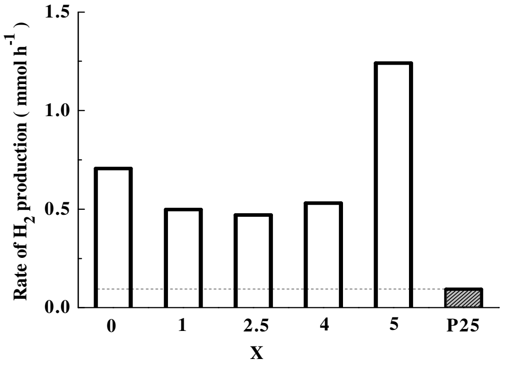

Figure 8. Formation rates of hydrogen over $Sr_2KNb_{5-x}Ta_xO_{15}$ with x= 0, 1, 2.5, 4 and 5 nanorod photocatalysts (Conditions: 0.1 g of photocatalysts; 50 mL of methanol dissolved in 500 mL of water, 500 W Hg lamp).

Photocatalytic Overall Water Splitting

All native photocatalysts did not possess photocatalytic activity in pure water, probably due to the low charge separation and transfer efficiency. While 1.0 wt% NiO_x was loaded as co-catalyst, the photocatalytic overall water splitting into stoichiometric amounts of H_2 and O_2 can be effectively promoted over prototypical examples of $Sr_2KNb_5O_{15}$ and $Sr_2KTa_5O_{15}$ photocatalysts. Figure 9 shows the time course of H_2 and O_2 evolution from pure water over 1.0 wt% $NiO_x/Sr_2KNb_5O_{15}$ and 1.0 wt% $NiO_x/Sr_2KTa_5O_{15}$ photocatalysts under UV light irradiation for 5 h. After some short induction period of about 15 minutes of irradiation, the formation of H_2 and O_2 in a stoichiometric ratio ($H_2/O_2 \approx 2/1$) was observed and there was no appreciable decrease by on-line monitoring of gas evolution, indicating that the samples are stable under UV light irradiation. Therefore, it is demonstrated that the presence of the double-layered nano-NiO_x particles as co-catalysts on the surface of photocatalysts can improve the photocatalytic activity for overall water splitting. Based on the above TEM results, the formation of a Ni metal core at the surface of photocatalyst results in the formation of a Schottky contact at the interface, and thus facilitate electron transport to the NiO shell and suppress the backward reaction of water formation, leading to an enhancement of photocatalytic activity for overall water splitting.[35-38] Furthermore, the average rates of H_2/O_2 evolution over $Sr_2KNb_5O_{15}$ and $Sr_2KTa_5O_{15}$ photocatalysts were estimated to be about 36.2/15.2 and 84.5/46.3 μmol/h, respectively, thus the latter was more than 2 times higher than the former, in agreement with the above-presented comparison value from photocatalytic H_2 production by methanol reforming. These experimental results not only proved the photocatalytical abilities of the tunnel structured photocatalysts for overall water splitting, but also consistently confirmed the above reasonable prediction resulting from the theoretical calculation of the band structures.

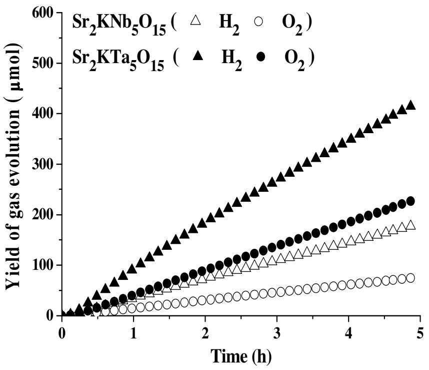

Figure 9. H_2 and O_2 evolution from pure water over 1.0 wt% NiO_x loaded $Sr_2KNb_5O_{15}$ and $Sr_2KTa_5O_{15}$ for 5 h (Conditions: 0.1 g of photocatalysts; 500 mL of H_2O, Hg lamp).

Conclusions

The novel $Sr_2KNb_5Ta_{5-x}O_{15}$ nanorod photocatalysts with tunnel structure were prepared by molten salt technique for 2 h at 850°C. The effective improvement of the photocatalytic H_2 production activity by Ta substitution has been demonstrated in methanol reforming. Compared to a bulk TiO_2 sample, the $Sr_2KNb_5Ta_{5-x}O_{15}$ nanorod photocatalysts showed much higher activity. Moreover, by loading of NiO_x co-catalyst on prototypical $Sr_2KNb_5O_{15}$ and $Sr_2KTa_5O_{15}$ photocatalysts, the decomposition of water into H_2 and O_2 at a stoichiometric amount (≈ 2:1) under UV irradiation was observed, which can be attributed to the improved charge separation and transfer in the presence of double-layer structure NiO_x co-catalyst. Therefore, it can be concluded that the tunnel structure photocatalysts are a new type of photocatalyst materials for overall water splitting from the view point of the tunable components because it consists of three different tunnels and octahedral arrays. Our ongoing work will continue to study on band gap engineering by controlling cation filling of three different tunnels and octahedral arrays, for extending the photosensitivity of photocatalytic oxides into the visible-light region.

Acknowledgements

We greatly appreciate Prof. Dr. M. Muhler (RUB, Germany) for his support, Dr. T. Reinecke (RUB, Germany) for XRD measurements. P.W. thanks for the scholarship support from the China Scholarship Council (CSC No.2011614004). R.M. gratefully acknowledges funding in the Emmy-Noether program (MA 5392/3-1) of the German Science Foundation DFG.

Notes and references

[a] *Laboratory of Industrial Chemistry, Faculty of Chemistry and Biochemistry, Ruhr-University Bochum, Universitaetsstrasse 150, 44801 Bochum, Germany*
[b] *Institute of Physical Chemistry, Justus-Liebig-University Giessen, Heinrich-Buff-Ring 58,35392 Giessen, Germany*
[c] *Institute for Chemistry, Technical Chemistry, Carl von Ossietzky University Oldenburg, Carl-von-Ossietzky-Str. 9-11, 26129 Oldenburg, Germany. Tel: +49 441 798 3675; Fax: +49 441 798 3330; E-mail: michael.wark@uni-oldenburg.de*

1. P. Yang and J. M. Tarascon, *Nat. Mater.*, 2012, **11**, 560.
2. A. J. Bard and M. A. Fox, *Acc. Chem. Res.*, 1995, **28**, 141.
3. S. T. Martin, A. T. Lee and M. R. Hoffmann, *Environ. Sci. Technol.*, 1995, **29**, 2567.
4. F. E. Osterloh, *Chem. Mater.*, 2008, **20**, 35.
5. A. Kudo and Y. Miseki, *Chem. Soc. Rev.*, 2009, **38**, 253.
6. X. B. Chen, S. H. Shen, L. J. Guo and S. S. Mao, *Chem. Rev.*, 2010, **110**, 6503.
7. Y. Miseki, H. Kato and A. Kudo, *Energy Environ. Sci.*, 2009, **2**, 306.
8. M. Kohno, T. Kaneko, S. Ogura, K. Sato and Y. Inoue, *J. Chem. Soc., Faraday Trans.*, 1998, **94**, 89.
9. S. Ogura, M. Kohno, K. Sato and Y. Inoue, *Appl. Surf. Sci.*, 1997, **121**, 521.
10. A. Magneli and B. Blomberg, *Acta Chem. Scand.*, 1951, **5**, 372.
11. A. Simon and J. Ravez, *CR. Chim.*, 2006, **9**, 1268.
12. S. Lanfredi, C. X. Cardoso and M. A. L. Nobre, *Mater. Sci. Eng. B*, 2004, **112**, 139.
13. E. Garcia-Gonzalez, A. Torres-Pardo, R. Jimenez and J. M. Gonzalez-Calbet, *Chem. Mater.*, 2007, **19**, 3575.
14. M. Prades, N. Maso, H. Beltran, E. Cordoncillo and A. R. West, *Inorg. Chem.*, 2013, **52**, 1729.
15. J. J. Wu, F. Q. Huang, Z. C. Shan and Y. M. Wang, *Dalton Trans.*, 2011, **40**, 6906.
16. L. W. Zhang, H. B. Fu, C. Zhang and Y. F. Zhu, *J. Phys. Chem. C*, 2008, **112**, 3126.
17. S. M. Zhang, G. K. Zhang, S. J. Yu, X. G. Chen and X. Y. Zhang, *J. Phys. Chem. C*, 2009, **113**, 20029.
18. O. Palasyuk and P. A. Maggard, *J. Solid State Chem.*, 2012, **191**, 263.
19. P. Wang, P. Chen, A. Kostka, R. Marschall and M. Wark, *Chem. Mater.*, 2013, **25**, 4739.
20. K. Domen, A. Kudo, T. Onishi, N. Kosugi and H. Kuroda, *J. Phy. Chem.*, 1986, **90**, 292.
21. X. Wang, Q. Xu, M. R. Li, S. Shen, X. L. Wang, Y. C. Wang, Z. C. Feng, J. Y. Shi, H. X. Han and C. Li, *Angew. Chem. Int. Edit.*, 2012, **51**, 13089.
22. L. Schwertmann, M. Wark and R. Marschall, *Rsc Adv.*, 2013, **3**, 18908.
23. R. D. Shannon, *Acta Crystallogr. A*, 1976, **32**, 751.
24. C. Duran, G. L. Messing and S. Trolier-Mckinstry, *Mater. Res. Bull.*, 2004, **39**, 1679.
25. Z. P. Yang, L. L. Wei, Y. F. Chang and B. Liu, *J. Mater. Sci.*, 2007, **42**, 3627.
26. Z. P. Yang, L. L. Wei and Y. F. Chang, *J. Eur. Ceram. Soc.*, 2007, **27**, 267.
27. L. L. Wei, Z. P. Yang, Y. F. Chang and R. I. Gu, *J. Am. Ceram. Soc.*, 2008, **91**, 1077.
28. L. Wei, Z. Yang, H. Ren and X. Chen, *J. Am. Ceram. Soc.*, 2010, **93**, 3986.
29. Z. P. Yang, R. Gu, L. L. Wei and H. M. Ren, *J. Alloy. Compd.*, 2010, **504**, 211.
30. Z. P. Yang, Y. F. Chang and L. L. Wei, *Appl. Phys. Lett.*, 2007, **90**.
31. D. Arney, C. Hardy, B. Greve and P. A. Maggard, *J. Photochem. Photobiol. A*, 2010, **214**, 54.
32. N. McLamb, P. P. Sahoo, L. Fuoco and P. A. Maggard, *Cryst. Growth Des.*, 2013, **13**, 2322.
33. D. E. Scaife, *Sol. Energy*, 1980, **25**, 41.
34. B. Siritanaratkul, K. Maeda, T. Hisatomi and K. Domen, *ChemSusChem*, 2011, **4**, 74.
35. M. Tian, W. Shangguan, J. Yuan, S. Wang and Z. Ouyang, *Sci. Technol. Adv. Mater.*, 2007, **8**, 82.
36. Y.-C. Chiou, U. Kumar and J. C. S. Wu, *Appl. Catal. A: Gen.*, 2009, **357**, 73.
37. Z. Zou, J. Ye, K. Sayama and H. Arakawa, *Nature*, 2001, **414**, 625.
38. T. K. Townsend, N. D. Browning and F. E. Osterloh, *ACS nano*, 2012, **6**, 7420.

Graphical abstract